Dual-loaded Drugs and Controlled Release based on Self-transforming Microneedle

Kim, Hyunjae

Department of Medical Device Engineering and Management
Graduate School
Yonsei University

Dual-loaded Drugs and Controlled Release based on Self-transforming Microneedle

Advisor Sung, Hak-joon

A Master's Thesis Submitted
to the Department of Medical Device Engineering and
Management and the Committee on Graduate School
of Yonsei University in Partial Fulfillment of the
Requirements for the Degree of
Master of Engineering

Kim, Hyunjae

June 2025

Dual-loaded Drugs and Controlled Release based on Self-transforming Microneedle

This Certifies that the Master's Thesis
of Kim, Hyunjae is Approved

Committee Chair	**Sung, Hak-joon**
Committee Member	**Cho, Sungwoo**
Committee Member	**Lee, Kang Suk**

Department of Medical Device Engineering and Management
Graduate School
Yonsei University
June 2025

TABLE OF CONTENTS

LIST OF FIGURES

ABSTRACT

Dual-loaded Drugs and Controlled Release based on Self-transforming Microneedle

Advancements in drug delivery technologies, such as autoinjectors and implantable devices (e.g., Implanon, Norplant), have led to patient-friendly innovations. In this study, self-transforming microneedles (SMNs) were developed as a targeted drug delivery system for infertility treatment, enabling high-capacity drug loading and controlled hormone release. A dual-layered SMN system including gelatin methacryloyl (GelMA) was designed to achieve controlled drug release kinetics via shape memory properties. Additionally, finite element analysis (FEA) was used to optimize the structural design, determining the ideal slot configuration for enhanced skin penetration efficiency. After insertion, the outer layer, loaded with follicle-stimulating hormone (FSH) gradually degrades, continuously releasing the drug over three days. This process enables multiple follicles to mature simultaneously. Upon thermal stimulation, the microneedles recover their original shape, triggering the burst release of human chorionic gonadotropin (hCG) from the inner layer within one day, thereby inducing ovulation. The efficacy of this SMN-based drug delivery system was validated through a series of *in vitro* and *ex vivo* experiments. In particular, *in vitro* release and subsequent bioactivity assays validated the drug's functional efficacy, demonstrating its potential as a targeted and controllable hormone delivery platform.

Key-words : **Microneedle, Shape Memory Polymer, Self-transformation, Dual-loaded drug, Controlled release**

1. INTRODUCTION

Modern society's trend of postponing marriage and childbearing has elevated infertility rates which subsequently triggered a higher need for assisted reproductive technologies (ART). Infertility is defined by the inability to conceive after regular unprotected sexual intercourse which impacts 10-15% of couples worldwide making it a significant public health issue. [1,2] Patients suffering from infertility encounter psychological distress because they cannot conceive which motivates ongoing research and development of treatments.[3]

A common method for treating reproductive infertility is to use an injection of follicle stimulating hormone (FSH), which plays a role in inducing the maturation of ovarian follicles and human chorionic gonadotropin (hCG), which promotes the rupture of the follicles and ovulation after the follicles have matured.[4,5] Such gonadotropin stimulation treatment plays a crucial role in ART, such as in vitro fertilization (IVF) and intracytoplasmic sperm injection (ICSI) by inducing ovarian stimulation to produce oocytes, followed by fertilization and embryo transfer.[6-9]

However, gonadotropin stimulation treatment typically relies on frequent injections, significantly impacting patient comfort and compliance. Patients often experience physical discomfort, including pain, bruising, and inflammation at injection sites, especially with subcutaneous or intramuscular administration. [10-12] Repeated injections also inherently carry risks such as infections, potentially causing complications both locally and internally. Additionally, many patients face practical and psychological challenges due to unfamiliarity with proper self-injection techniques or overwhelming needle anxiety, a condition characterized by intense fear of injections, affecting approximately 10% of the global population and often causing delays or avoidance of necessary medical treatments.[13-15] To overcome these issues, there is growing interest in developing painless, minimally invasive drug delivery systems that can enhance patient comfort, minimize complications like nerve damage from incorrect administration, and alleviate psychological barriers associated with needle anxiety.[16,17]

In this study, a minimally invasive, painless, and biocompatible microneedle-based drug delivery system is developed specifically for infertility patients experiencing needle anxiety. To fabricate a minimally invasive microneedle, we used a polycaprolactone (PCL) based shape memory polymer (SMP). SMPs are a class of smart materials that can be programmed to have a specific shape under a certain condition such as body temperature, returning to the original shape from temporary shape under the given identical condition. Recently, PCL-based SMPs have been widely used in the development of implantable medical devices, such as nasolacrimal stents, vascular stents, hernia meshes, and scaffolds. [18-21]

SMN optimize drug-loading capacity through specialized structural designs that simultaneously deliver multiple drugs, effectively reducing injection frequency.[22] SMN structure featuring specialized slots is developed to maximize drug-loading capacity. [23] Computational finite element analysis evaluates the structural integrity and skin penetration capabilities, ensuring practical effectiveness. When delivering ovarian stimulation drugs through microneedle, careful control of dosage and timing is essential for successful induction of ovulation and optimal ovarian response. [24,25] The shape-memory characteristics of selected polymers are analyzed, alongside the mechanical strength and degradation profiles of hydrogels, which are optimized through adjustments in crosslinking point and concentration. [26,27] Degradation test identifies the optimal hydrogel formulations suitable for sustained or burst drug release. FSH is loaded onto the outer layer of the microneedles for sustained release to facilitate ovarian follicle maturation. hCG is encapsulated within the inner layer for burst release upon shape transforming to trigger ovulation. This innovative approach seeks to maintain the therapeutic effectiveness of traditional gonadotropin injections while significantly reducing physical discomfort and stress.

2. MATERIALS AND METHODS

2.1. Finite Element Analysis (FEA)

The 3D mesh model was created using Finite Element Analysis (FEA) combined with Computer-Aided Design software (CAD, Fusion 360, Autodesk Inc., version 2018, California, USA), and stress distribution under directional displacement was subsequently simulated using the Explicit Dynamics module in Ansys Workbench (ANSYS 2020R1, ANSYS, Canonsburg, PA, USA).

To replicate human skin, A tri-layered skin model was developed, comprising a stratum corneum (top layer, 20 μm thick), an epidermis (middle layer, 80 μm thick), and a dermis (bottom layer, 1,500 μm thick). Additionally, a stimulated skin model with a 1 mm diameter was presented.

Microneedle-skin interactions were analyzed using explicit dynamics simulation, comparing three different slot-based designs: a 3-slot (n = 3), 4-slot (n = 4), and 5-slot (n = 5) configuration, where n indicates the number of slots. Microneedle geometry parameters (length, base diameter, and tip diameter), skin material properties, and displacement (700 μm) were maintained consistently across simulations to determine the optimal external design appropriate for the intended purpose. The skin layer was evaluated based on the Explicit Dynamics reaction force (or stress) and insertion depth, determining whether penetration extended beyond the dermis. The analysis considered the x-, y- and z-axis components.

2.2. Synthesis of SMP

The synthesis of SMP was carried out via a ring-opening polymerization method utilizing ε-caprolactone (CL) and glycidyl methacrylate (GMA) monomers. [20] Briefly, CL (315 mmol), dipentaerythritol (0.5 mmol), and hydroquinone (3.5 mmol; hydroquinone to GMA molar ratio = 1:10) were first reacted in a three-necked round-bottom flask at 110℃ for 10 min, with hydroquinone serving as an inhibitor to prevent auto-crosslinking. Subsequently, GMA (35 mmol) was added to the mixture and stirred for an additional 10 min. Following this step, 1,5,7-Triazabicyclo[4.4.0]dec-5-ene (TBD; 1 mmol) was dissolved in 4 mL of acetonitrile and subjected to reaction at 110°C for 6 h under a nitrogen atmosphere. After the mixture was cooled to room temperature (25°C), the resulting product was fully dissolved in chloroform (30 mL). The addition of this chloroform solution into chilled diethyl ether (800 mL, 4°C) resulted in the precipitation of a white solid. Finally, the SMP was collected and dried under vacuum at room temperature using an

OV4-30 dryer. (Jeio Tech, Daejeon, Republic of Korea). The resulting product, 6-arm 94% polycaprolactone-co-06% polyglycidyl methacrylate (94% PCL-06% PGMA), was synthesized. To enhance stiffness, the material was blended with polycaprolactone. PCL (Mn = 80,000, Sigma–Aldrich) in a weight ratio of 20:80 (PCL: SMP). All chemicals were purchased through Sigma-Aldrich (St. Louis, MO, USA).

2.3. Preparation and characterization of SMP-PCL by solution blending

SMP-PCL sample with PCL content of 10 wt% was prepared by solution mixing using chloroform as a solvent. SMP (30 g) was dissolved in chloroform ($CHCl_3$; 200ml, Samchun) at 40℃, with the addition of 2-hydroxy-1-(4-(hydroxyethoxy)phenyl)-2-methyl-1-propanone (Irgacure 2959; 5 mg, Sigma-Aldrich) serving as a photo-initiator. PCL (Mn = 80,000, Sigma–Aldrich) was then blended in equal volumes (1:1, v/v) and stirred continuously for 1 h to ensure homogeneity after which was poured into the petri dish covered with polytetrafluoroethylene film (CoValue, Cheonan, Republic of Korea) and dried on a hood bench for 24 h.

The thermochemical property of SMP-PCL was characterized by differential scanning calorimetry (DSC; Discovery DSC25, TA Instruments, New Castle, DE, USA). First, Heat-flow-related thermal transitions were examined using DSC. The samples were heated to 150℃, and then cooled to –80℃ for two cycles at a heating rate of 10℃min–1 under a nitrogen atmosphere. The glass transition temperature (T_g), melting temperature (T_m) and crystallization temperature (T_c) were determined using DSC thermograms.

2.4. Fabrication of SMN

SMN was designed using CAD software (Fusion360, Autodesk) as a 3D structure and converted into layered 2D images for fabrication by the digital light processing 3D printer (S240, Boston Micro Fabrication Material Technology Inc., Shenzhen, China). The S240 machine (BMF Precision Technology Ltd., China) provides high-resolution printing with 10 μm resolution along both the x- and y-axes and a layer thickness of 10 μm. The printed molds were immersed in ethanol at ambient temperature and subjected to ultrasonic cleaning for 5 min to eliminate residual resin. After cleaning, the mold underwent additional curing under UV exposure for 10 min to enhance mechanical strength. The 3D-printed molds were subsequently used to create negative molds via soft molding technique, employing polydimethylsiloxane (PDMS; SYLGARD 184 Silicone Elastomer, DOW Corning, Michigan, USA) mixed at a 10:1 (base to curing agent) ratio.

SMNs were fabricated by a molding process. The SMP–PCL blended samples were compression-molded into a PDMS master mold at 100 °C under 10 MPa for 10 min. After molding, the samples were immediately placed on ice for 10 min to fix the cone shape, followed by UV crosslinking to program the SMNs into the desired cone-shaped form. Next, thermal programming was conducted by heating above the melting temperature (T_m), then remolding them into the X-shaped master mold using the same compression process and ice fixation to obtain the X form of SMN.

Initially, the microneedle takes its original shape, referred as Shape C, featuring a conical structure with a base diameter of 400 μm and a height of 700 μm. A microneedle array (21 × 21) was fabricated with a center-to-center spacing of 1 mm between adjacent microneedles. To enable drug loading, the microneedle undergoes shape programming and is temporarily transformed into Shape X– a configuration characterized by an X-shaped cross-section with a reduced base diameter of 200 μm and integrated slots, while maintaining the same height of 700 μm.

2.5. Synthesis of Gelatin Methacryloyl (GelMA)

GelMA was synthesized by chemically modifying gelatin through the reaction between its amine groups and methacrylate groups. [28,29] Briefly, porcine skin gelatin powder (20 g; gel strength 300, type A, Sigma-Aldrich) was completely dissolved in phosphate-buffered saline (PBS; 1X, pH 7.4, Welgene, Gyeongsangbuk-do, Republic of Korea) at 40°C to prepare a 10% (w/v) gelatin solution. Methacrylic anhydride (MA; 2 mL per 10% gelatin solution) was then added dropwise at a flow rate of 0.5 mL/min into 200 mL of the gelatin solution and allowed to react under vigorous stirring at 50°C in the dark for 3 h. The reaction was terminated by adding a five-fold volume of warm PBS (40°C). Unreacted MA and salts were removed by dialysis against warm deionized water (40°C) for 5 days in the dark, using dialysis tubing with a molecular weight cut-off (MWCO) of 12–14 kDa (Spectrum Laboratories Inc., New Brunswick, NJ, USA). After dialysis, the GelMA solution was lyophilized to obtain a white porous foam, which was stored at −30°C until further use.

2.6. Structural analysis of SMP and GelMA

Proton nuclear magnetic resonance spectroscopy (^{1}H-NMR; Avance III 400 MHz, Bruker Biospin, Billerica, MA, USA) was employed to confirm successful synthesis of SMP and GelMA.

For analysis, SMP sample was dissolved in deuterated chloroform ($CDCl_3$; Sigma-Aldrich) and GelMA sample was dissolved in deuterated dimethyl sulfoxide (DMSO-d_6; Sigma-Aldrich).

2.7. Preparation of Drug-loaded SMN

A 10% (w/v) GelMA solution was prepared by dissolving 20 mg of GelMA(Sigma-Aldrich) in saline and a drug solution (total volume: 200 µL) containing hCG (IVF-C, 5000 IU/vial, LG Chem, Seoul, Republic of Korea) and FSH (IVF-M HP Multidose, 6000 IU/vial, LG Chem, Seoul, Republic of Korea), adjusting the drug concentration to achieve a total activity of 225 IU. Pluronic F-127 (Sigma-Aldrich) was added at a final concentration of 0.03% (w/v) to enhance drug stability and regulate degradation time. Lithium phenyl-2,4,6-trimethylbenzoylphosphinate (LAP; Sigma-Aldrich, 0.2 µg) was added as a photo-initiator. The mixture was stirred at 60℃ for 2 h until homogeneously mixed and subsequently used for further experiments. The casting method was used to coat microneedles with GelMA. First, the GelMA solution was poured into the PDMS reverse mold, and GelMA solution was distributed in the mold at 3,000 rpm for 5 min at 40℃. After that, uncoated SMN was inserted, and UV with a wavelength of 405 nm was irradiated to induce a cross-linking reaction, through which the GelMA hydrogel was coated on the microneedles. The coated SMN was stored at 4℃ for 3 h before use.

2.8. Scanning Electron Microscopy (SEM)

The SMN surface was imaged by Field-emission Scanning Electron Microscopy (FE-SEM, JEOL Ltd., Tokyo, Japan) upon sputter-coating with a thin platinum layer by accelerating the voltage to 15 kV.

2.9. Atomic Force Microscopy (AFM)

The roughness of MN was examined by AFM (NX-10, Park Systems Corp., Gyeonggi-do, Republic or Korea) with the position adjustment of probe (Standard Contact Mode AFM Probe, Probes, Seoul, Republic of Korea). The surface was scanned by moving the AFM tip in a raster pattern to record height data, thereby creating a surface topographical map. The average roughness

(R_a), root mean square roughness (R_q), and peak-to-valley distance (R_t) were analyzed through multiple scans for statistical relevance. The significance of roughness parameters was assessed in the context of the 2D film properties considering the requirement of AFM imaging.

2.10. Water Contact Angle

Water contact angle and surface energy of polymer surface were determined on films (thickness: 1 mm) using a Contact Angle Meter-2 (DSA 25; Kruss, Hamburg, Germany). Deionized water or diiodo-methane (1-2 uL) was dropped under 22-25°C, followed by the measurement within 10 s. Using the software of contact angle meter, the air phase angle between the water droplet and the surface was determined by fitting a tangent line from the droplet boundary to the surface.

2.11. Cross-cut adhesion

SMN samples were prepared in two configurations: Shape X was characterized by rough surface morphology, whereas Shape C demonstrated smooth surface characteristics achieved through shape recovery processing. Then, SMNs were coated with GelMA in rhodamin B (Rho B, Sigma–Aldrich). After coating, the surface was cross-cut into a 7 × 14 grid using a scalpel blade. A cellophane film tape (adhesion strength: 1.219kg/in, ISO 2409) was then applied and subsequently peeled off.

2.12. Shape Memory Property

Shape memory properties were examined by programming with SMN. Shape C (Cone form) microneedle was heated using a heat gun at 55°C ($T > T_m$). Then, it was deformed into a Shape X(X-form) using a PDMS mold and fixed in shape at 4°C. Subsequently, the SMN was reheated above 55°C to induce shape transforming, returning to its original Shape C*(recovered cone form). After transforming, the base diameter of the microneedles was measured. The degree of shape transforming was quantified using Equation (1), calculating the shape transforming ratio (%) for individual microneedles using ImageJ. (n=30, each group)

$$\text{Shape transforming ratio per single microneedle (\%)} = (D_{transforming}/D_{original}) \times 100 \text{ --- (1)}$$

$D_{transforming}$ represents the diameter of the recovered cone form (Shape C), while $D_{original}$ corresponds to the diameter of the initial cone form (shape C).

2.13. Visualization of multilayer-SMN

SMNs were coated with GelMA containing RhoB as the inner layer and GelMA loaded with fluorescein isothiocyanate–dextran (FITC, Sigma-Aldrich) as the outer layer. The multilayered microneedles were sectioned and observed using confocal microscope (LSM 980; Zeiss, Oberkochen, Land Baden-Wurttemberg, Germany).

2.14. Skin Penetration Analysis

New Zealand White rabbit skins (female, 8 weeks old) were obtained from DooYeol Biotech (Seoul, Republic of Korea), rinsed in deionized water, shaved and trimmed of fat using a scalpel. The SMNs were then inserted into the skin blocks of a rabbit under gentle thumb pressure for 5 mins. To induce the shape memory effect, warm water at approximately 50°C was poured over the area, after which the microneedles were removed. The skins samples were fixed with 4% paraformaldehyde (PFA; CellNest) overnight at 4°C followed by embedding in paraffin wax. The paraffin blocks were then sectioned into 4 μm-thick slices using a microtome (HistoCore Multicut; Leica Microsystems, Wetzlar, Germany) and subjected to Hematoxylin & Eosin (H&E) staining following the manufacturer’s instructions. Additionally, rabbit skin blocks were stained with trypan blue (Sigma-Aldrich) for 20 mins. After wiping off the remaining dye, the samples were imaged using a stereo microscope (SMZ745T; Nikon, Tokyo, Japan).

2.15. Degradation of GelMA

GelMA hydrogels with uniform cylindrical shapes (8 mm diameter × 1 mm height) were fabricated at two concentrations (5% and 10% w/v) through UV crosslinking using a cylindrical mold (n = 3). For the in vitro degradation assay, the hydrogels were incubated in saline solution with type I collagenase (1 unit/mL; Gibco, Waltham, MA, USA) and maintained at 37°C on a rocking shaker (50 rpm, RK-1D, Daihan Scientific, Kangwon-do, Republic of Korea), and the saline was refreshed every 12 h. At each time point, remaining hydrogels were collected, rinsed twice with distilled water, lyophilized, and weighed. The percentage of remaining hydrogel mass was determined by applying the following equation (2) [30]:

$$\text{Weight (W\%) of non-degradation} = (W_{\text{each time point}}/W_{\text{starting point}}) \times 100 \text{ --- } (2)$$

2.16. FSH ELISA Assay

FSH concentrations were determined using a commercial ELISA kit, (Alpha Diagnostic International, Cat. 0200), according to the manufacturer’s instructions, with all reagents were adjusted to room temperature beforehand. A total of 25 uL of standards and GelMA release samples were introduced in duplicate into the wells of a 96-well plate previously covered with anti-human FSH antibody. The plate was incubated on a plate shaker at 200 rpm for 30 min at room temperature. Following incubation, the wells were washed three times with 300 µL of 1× wash buffer. Next, 100 µL of HRP-conjugated detection antibody was loaded into each well, followed by a 30-min incubation at room temperature. After washing the plate three times, 100 µL of TMB substrate solution was introduced into each well, followed by incubation of the plate in the dark for 15 min. The enzymatic reaction was then stopped by adding 50 µL of stop solution to each well. Absorbance was then read using a microplate reader set to 450 nm (e.g., SpectraMax i3, Molecular Devices). The standard curve was established based on known concentrations of FSH standards provided in the kit, and sample concentrations were calculated by interpolating from the standard curve.

2.17. hCG ELISA Assay

The concentration of hCG released from GelMA hydrogels was determined using a commercial ELISA kit (Human hCG ELISA Kit, Alpha Diagnostic International, Cat. No. 0400), following the manufacturer’s protocol. Prior to the assay, all reagents were brought to room temperature. GelMA release samples were obtained at scheduled time points and subjected to analyze either directly or after appropriate dilution with the assay buffer to ensure values fell within the standard curve range. A total of 25 µL of standards, controls, and release samples were applied in duplicate to wells of a pre-coated 96-well microtiter plate with anti-hCG antibody. Then, 100 µL of HRP-conjugated antibody solution (1:50 diluted) was added to each well and gently mixed. The plate was incubated at room temperature (25–28℃) on a plate shaker (approximately 200 rpm) for 60 min. After incubation, the wells were washed three times with 300 µL of 1× wash buffer. Subsequently, 100 µL of TMB substrate solution was added to each well. Following a 15-min incubation at room temperature, the enzymatic reaction was terminated by adding 50 µL of stop solution. Absorbance was read at 450 nm using a microplate reader (e.g., SpectraMax i3, Molecular Devices) within 15–30 min of stopping the reaction. Each sample's concentration was calculated by referencing the standard curve generated using known concentrations of hCG standards supplied with the kit.

2.18. Statistical Analysis

Data were presented as mean ± SD by denoting "n" as the number of samples obtained from distinct experiments. Dot-and whisker plots were also used by showing the corresponding averages and ranges of data. Each experiment was repeated at least three times, and data were analyzed using two-tailed Student's t-tests for pairwise comparisons and one-way analysis of variance (ANOVA) to determine statistically significant differences among group means. These differences were further analyzed by comparing multiple groups pair wise using Tukey's post-hoc test. Statistical significance was set at $p < 0.05$, with annotations for varying levels of significance (*$p < 0.05$, **$p < 0.01$, ***$p < 0.001$, and N.S.: no significant difference). Analysis was carried out using Excel, KyPlot 6.0 (Kyenslab, Tokyo, Japan), Origin 2018 (OriginLab, Northampton, MA, USA), and SigmaPlot V.12.0 (Systat Software Inc., San Jose, CA, USA).

3. RESULTS

3.1. Design and computational modeling of SMN with multi slots for enhanced drug loading

SMN designed with SMP, incorporating dual drug-loading of FSH on the outer layer for sustained release, and hCG within the inner layer for burst release upon shape transforming. (**Fig. 1-a**). The process of sequential drug release from the SMN begins with the sustained release of FSH from the outer layer, which gradually diffuses into the skin over the first 72 h to support ovarian follicle maturation. Around 72 h, the SMN undergo structural transformation through shape transforming, leading to the exposure of the inner layer containing hCG. This transformation triggers a burst release of hCG between 72 and 96 h, effectively inducing ovulation. This system ensures precise hormonal delivery, optimizing therapeutic outcomes for infertility treatment by integrating sustained and burst release mechanisms, (**Fig. 1-b**). Simulation of FEA was assessed the efficiency of different slot designs since slot volume directly influences drug-loading capacity in microneedles. In this context, slots refer to hollow spaces 9gwithin the microneedle structure that store and release drugs in a controlled manner. A comparison of 3-slot, 4-slot, and 5-slot designs was determined which configuration offers the largest drug-loading capacity. Total slot volume to load drug was analyzed that the 4-slot design provides the most extensive slot volume, providing it the most effective configuration for maximizing drug encapsulation and enhancing overall drug delivery efficiency (**Fig. 2**).

FEA stress distribution on SMN was compared using FEA in 3-slot, 4-slot, and 5-slot microneedle inserted (700 μm) into a skin-mimicking model under the same loading conditions. [31,32] The overall stress distribution on the microneedle surface shows that the 4-slot design experiences the lowest maximum stress and the most uniform distribution **(Fig. 3-a)**. In contrast, the 3-slot design displays a more irregular and concentrated stress pattern, indicating that certain regions may lack sufficient mechanical support, potentially leading to structural instability. The 5-slot design also demonstrates localized stress concentrations, particularly near the upper region. The cross-sectional stress distribution along the microneedle height further confirms that the 4-slot structure maintains a smoother stress gradient with fewer abrupt fluctuations **(Fig. 3-b)**. The maximum stress values for each configuration are quantitatively summarized, reinforcing that the 4-slot design achieves a favorable balance between stress magnitude and distribution **(Fig. 3-c)**.

Stress distribution during microneedle insertion was revealed distinct differences among slot designs. The 5-slot microneedle generated the highest stress concentration, indicating increased mechanical stress on the skin. In contrast, the 3-slot design exhibited the lowest stress but failed to achieve skin penetration. Although increasing the number of slots improves insertion efficiency, it also results in greater stress on surrounding tissue, which may affect insertion safety and user comfort (**Fig. 4-a**). The 4-slot design achieved effective penetration while minimizing stress on both the microneedle and the skin, offering a balanced mechanical performance (**Fig. 4-b**).

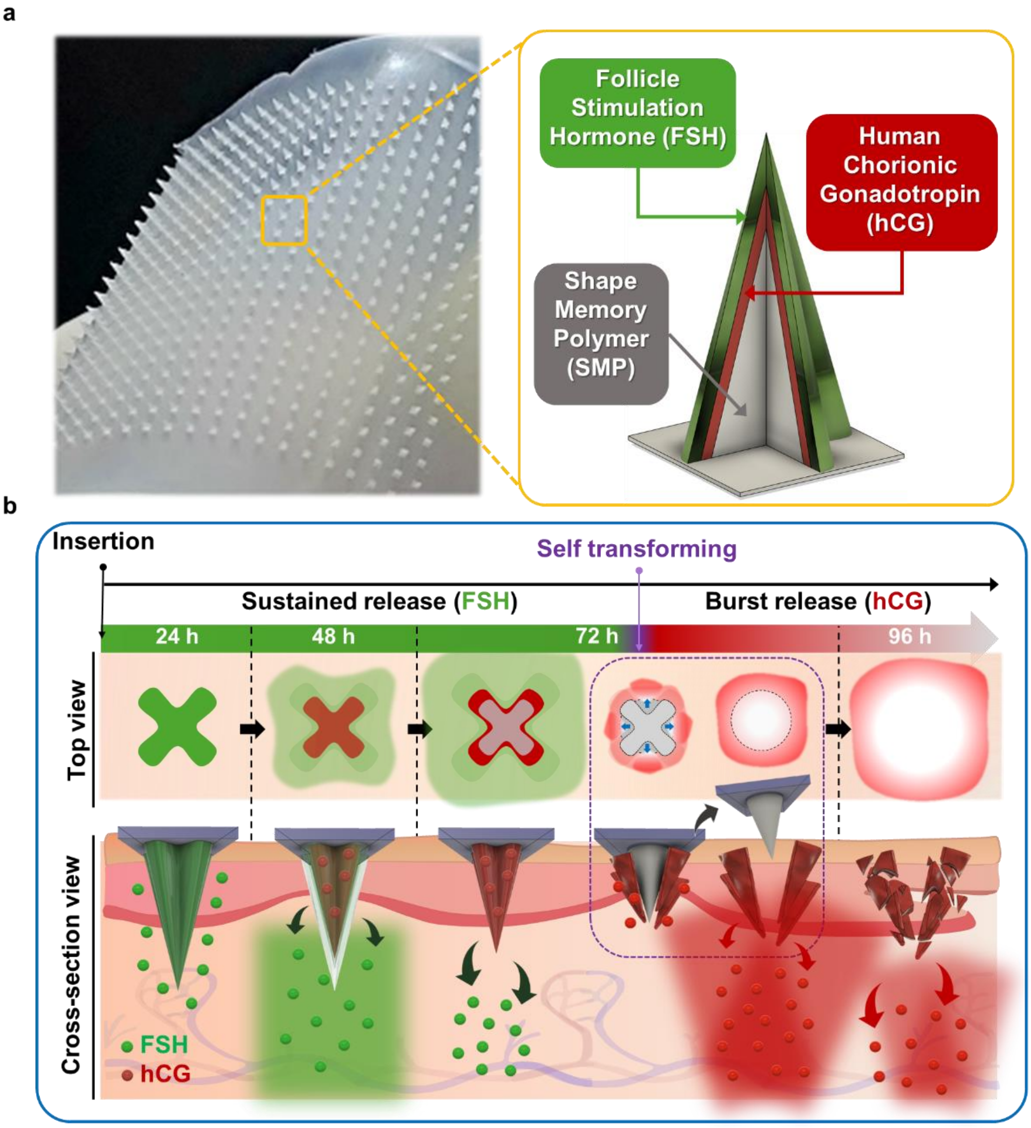

Figure 1. Schematic illustration of the SMN and its drug release mechanism. (a) The patch consists of a structured microneedle array made of SMP, with FSH coated on the outer layer and hCG encapsulated in the inner layer. (b) The drug release mechanism begins with the sustained release of FSH over 72 h, followed by shape transforming, which exposes the inner layer and triggers a burst release of hCG between 72 and 96 h, facilitating controlled hormone delivery.

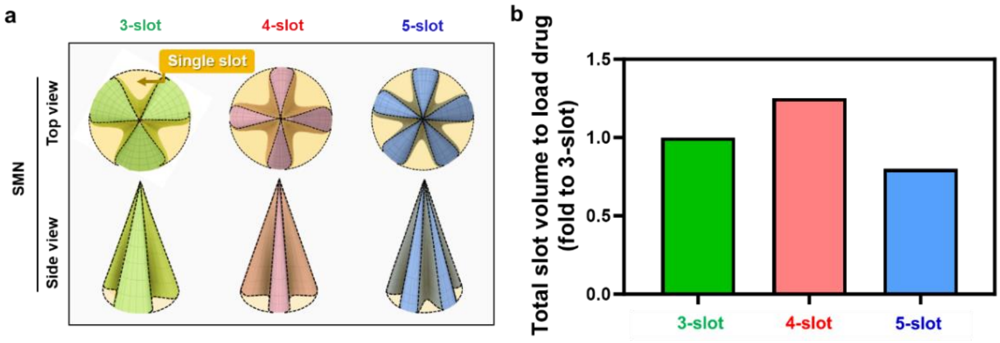

Figure 2. Multi-slot configuration of SMN and their corresponding drug-loading capacity. (a) Slots of microneedle with top and side views was displayed the structural differences and slot placements. (b) Quantitative analysis of the total volume using CAD and confirmed that the 4-slot design has the highest drug-loading capacity.

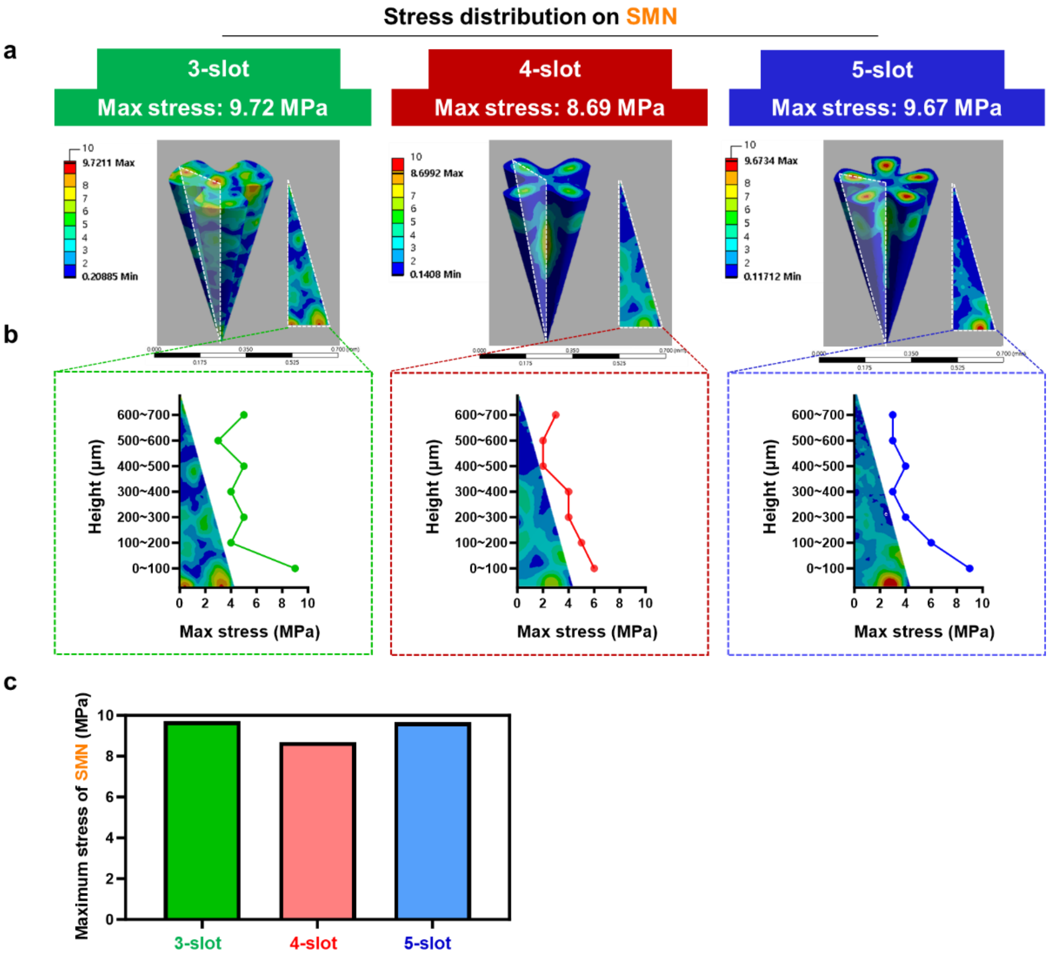

Figure 3. Stress distribution on SMN using FEA. (a) Representative stress contour plots illustrating localized stress concentrations within each microneedle geometry upon insertion. (b) Cross-sectional analysis of stress along the microneedle height, revealing distinct vertical stress patterns depending on slot configuration. (c) Quantitative comparison of maximum stress values (MPa) among the three designs, indicating comparable peak stress levels across configurations.

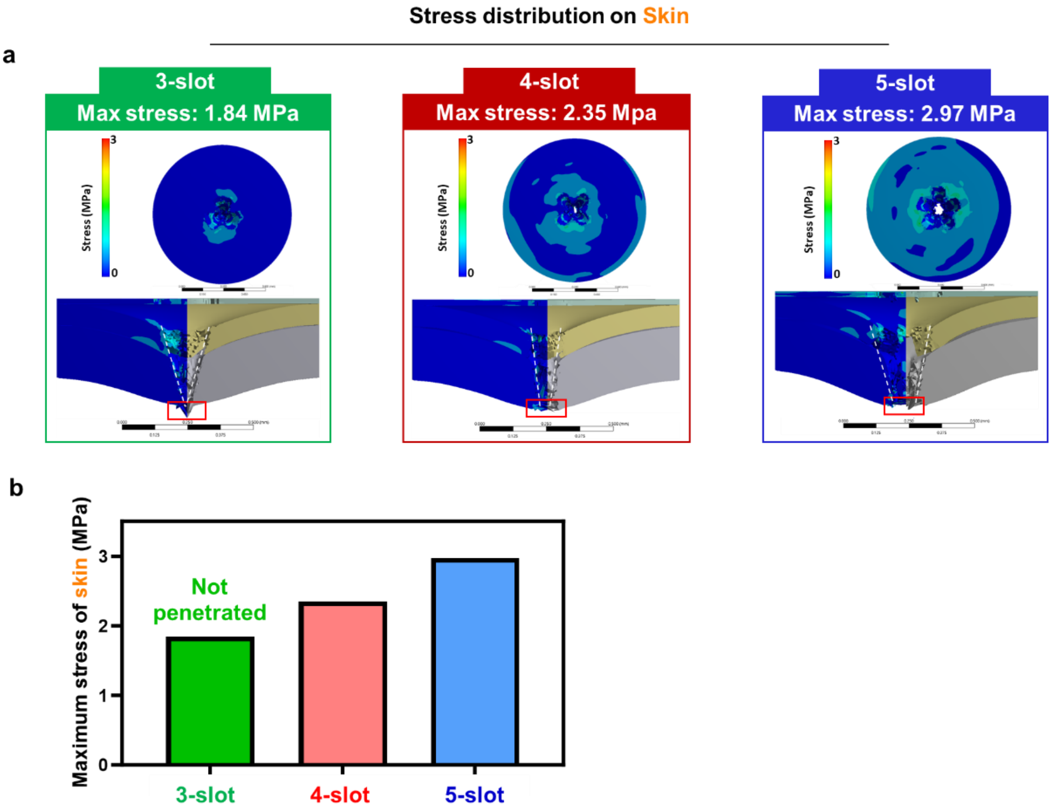

Figure 4. Stress distribution in skin by SMN. (a) Stress distribution map from the skin's viewpoint, highlighting localized deformation and stress intensity beneath each microneedle. (b) Quantification of the maximum stress values (MPa) within the skin by each microneedle configuration.

3.2. Shape memory properties and GelMA dual-loading

The 6arm structure shape memory structure (SMP) was synthesized by combining CL, GMA, and di-pentaerythritol through ring-opening polymerization. The methacrylate groups in SMP can be crosslinked and controls crystallinity and thermo-mechanical properties of polymer. (**Fig. 5-a**). The chemical structure of the synthesized SMP was examined by ^{1}H-NMR spectroscopy, showing characteristic peaks corresponding to the PCL and PGMA segments. The presence of methylene ($\delta \approx 1.4$–2.6 ppm, $-CH_2-$ from PCL and GMA) and vinyl ($\delta \approx 5.6$ and 6.1 ppm, $=CH_2$ from GMA) proton peaks confirmed the successful incorporation of both monomers. (**Fig. 5-b**) Additionally, thermal behavior of the SMP was evaluated using differential scanning calorimetry (DSC), which revealed a clear melting temperature (T_m), demonstrating its shape memory capability. Notably, the transition occurred below 40 ℃, suggesting that the SMP can be thermally activated under physiological conditions (**Fig. 5-c**). To visualize the functional mechanism of the SMN, the shape transformation and drug-loading/releasing process begins with the microneedle in its original cone form "Shape C". It is then programmed into temporary X form, known as "Shape X", which creates internal cavities for drug loading. After applying GelMA to encapsulate the loaded drug, forming what is called "Shape X*", the microneedle undergoes shape transforming, returning to its original cone form, referred to as "Shape C*", thereby enabling staged drug release (**Fig. 5-d**). Photo-crosslinkable GelMA was synthesized by chemically modifying gelatin through the reaction between its amine groups and methacrylate groups. UV exposure leads to the formation of a stable hydrogel network that can encapsulate drugs effectively (**Fig. 5-e**). Successful methacrylation was confirmed by ^1H-NMR spectroscopy. Compared to unmodified gelatin, the GelMA spectrum exhibited distinct peaks at $\delta \approx 5.4$–6.0 ppm, corresponding to the vinyl protons ($=CH_2$) of methacrylate groups. These signals were absent in the native gelatin spectrum, clearly indicating the successful introduction of methacrylate moieties into the gelatin backbone. (**Fig. 5-f**).

The appearance of SMN and shape transformation were confirmed using stereomicroscopy and SEM. The SMN successfully transitioned from their original cone form Shape C to a programmed Shape X, were then coated with GelMA, and ultimately returned to Shape C* through thermal transforming (**Fig. 6-a**). Since the height remained constant, transforming was quantitatively assessed by measuring the base diameter. The transforming ratio, calculated by comparing the diameters of the original and recovered cone shapes, reached 93%, demonstrating reliable shape memory performance (**Fig. 6-b**). The dual-layered drug loading was visualized using fluorescent dyes, with Rhodamine B in the inner GelMA layer and FITC in the outer layer. We confirmed clear separation of the two layers, showing successful bilayer encapsulation within the microneedle structure (**Fig. 6-c**).

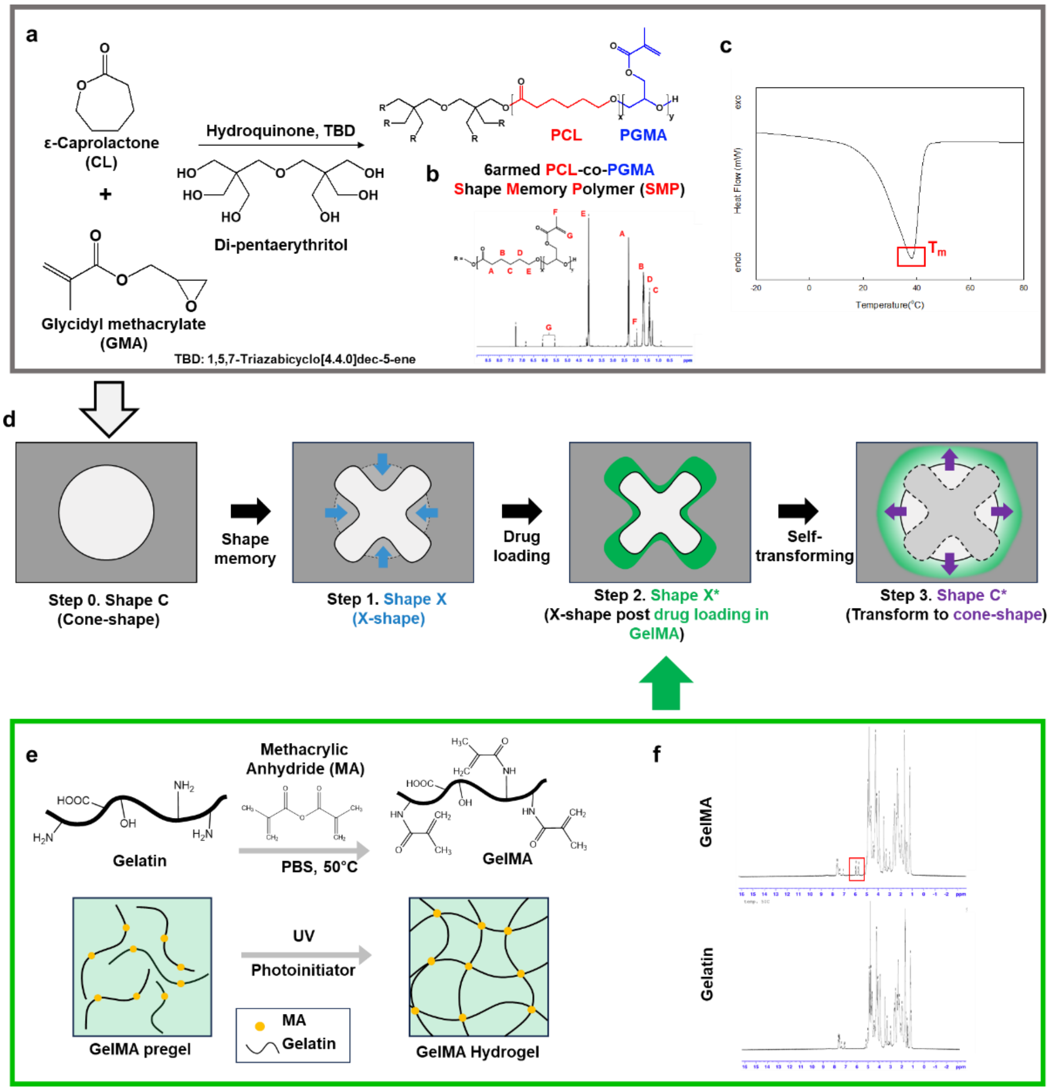

Figure 5. Overview of the fabrication and loading strategy for SMP and GelMA. (a) Synthesis of 6-armed PCL-co-PGMA. (b) ^{1}H-NMR spectrum of SMP. (c) DSC thermogram showing thermal transition (T_m: melting temperature). (d) The stepwise transformation of the SMN and its drug delivery mechanism are schematically represented. The fabrication of GelMA is also depicted in (e) and successfully confirmed by (f) H-NMR.

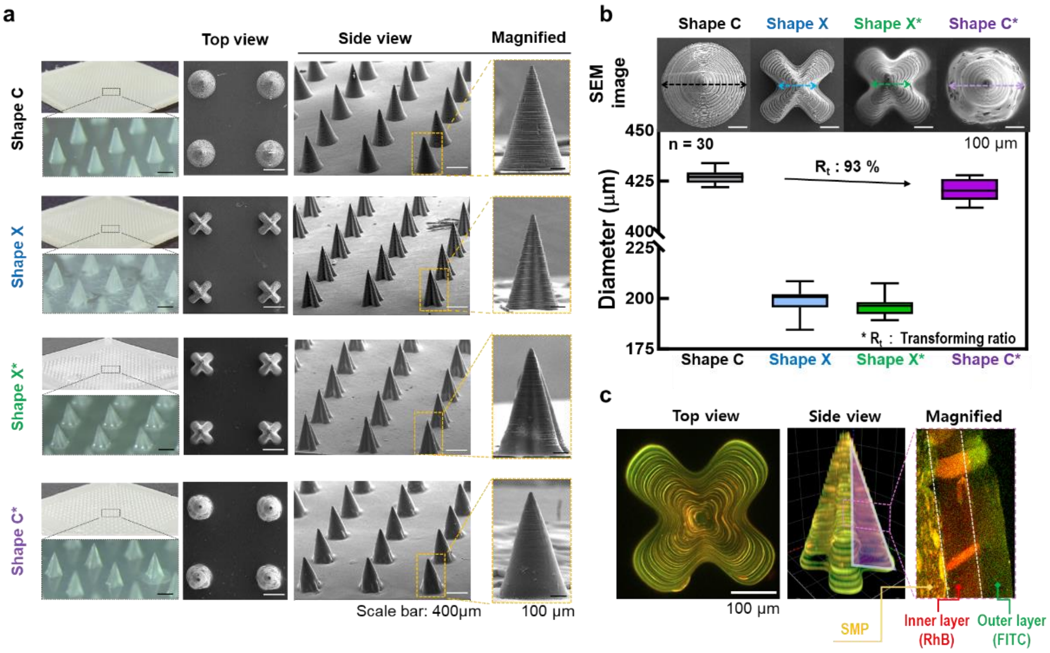

Figure 6. Characterization of the SMN. (a) Stereo-microscopic and SEM images showing the top and cross-sectional structures of the SMN. Scale bars, 400 μm (top, side) and 100 μm (magnified). (b) Single microneedle SEM images and base diameters measurements are presented, confirming the shape transforming performance. (c) To confirm the bilayer of structure, RhoB and FITC were stained and determined by confocal microscope. All data are shown as the mean ± S.D (n=30).

3.3. Surface Properties of SMN

Because GelMA acts as both a drug-loading and a release-controlling carrier [33], the surface morphology of SMN plays a critical role in modulating adhesion and detachment behavior. To understand this effect, the SMN were examined before and after heat-induced shape transformation (**Fig. 7-a**). SEM images showed that the Shape X configuration, prior to self-transformation, had ridges and grooves characteristic of PDMS mold, resulting in a rough surface suitable for GelMA coating. After heating at 45 °C, these features were largely smoothed out.

Surface changes were further assessed by AFM, which provided nanoscale measurements of microneedle topography. Surface roughness was notably reduced after self-transformation **(Fig. 7-b)**, indicating a smoother morphology. Water contact angle measurements **(Fig. 7-c)** supported this trend, with higher angles seen after self-transformation, reflecting reduced hydrophilicity and lower surface energy **(Fig. 7-d)**. The rough surface of Shape X exhibited greater surface energy due to the valley effect [34,35] – a phenomenon where microscopic valleys increase effective surface area and enhance hydrogel adhesion.

Next, the adhesion performance of the GelMA hydrogel coating on SMN surfaces was evaluated using a modified cross-cut test (ISO 2409) with commercial cellophane tape (1,218 g/inch, 3M 2400) **(Fig. 8-a)**. SMN in the Shape X and Shape C* states were uniformly coated with RhoB–loaded GelMA to enable visualization of residual hydrogel after testing. A 7 × 14 grid pattern was applied to each surface, and the tape was pressed and peeled vertically to assess coating retention. Visual imaging revealed stronger adhesion of GelMA on the rougher surface of Shape X, whereas substantial detachment occurred on the smoother Shape C* surface **(Fig. 8-b)**. Quantitative comparison of the remaining GelMA area indicated significantly higher retention on Shape X **(Fig. 8-c)**, suggesting that increased surface roughness enhances hydrogel adhesion through increasing surface area. Ultimately, the SMN enhances the adhesion of the drug coating and enables the drug to remain in the tissue through shape transformation during removal, while allowing easy extraction of SMN.

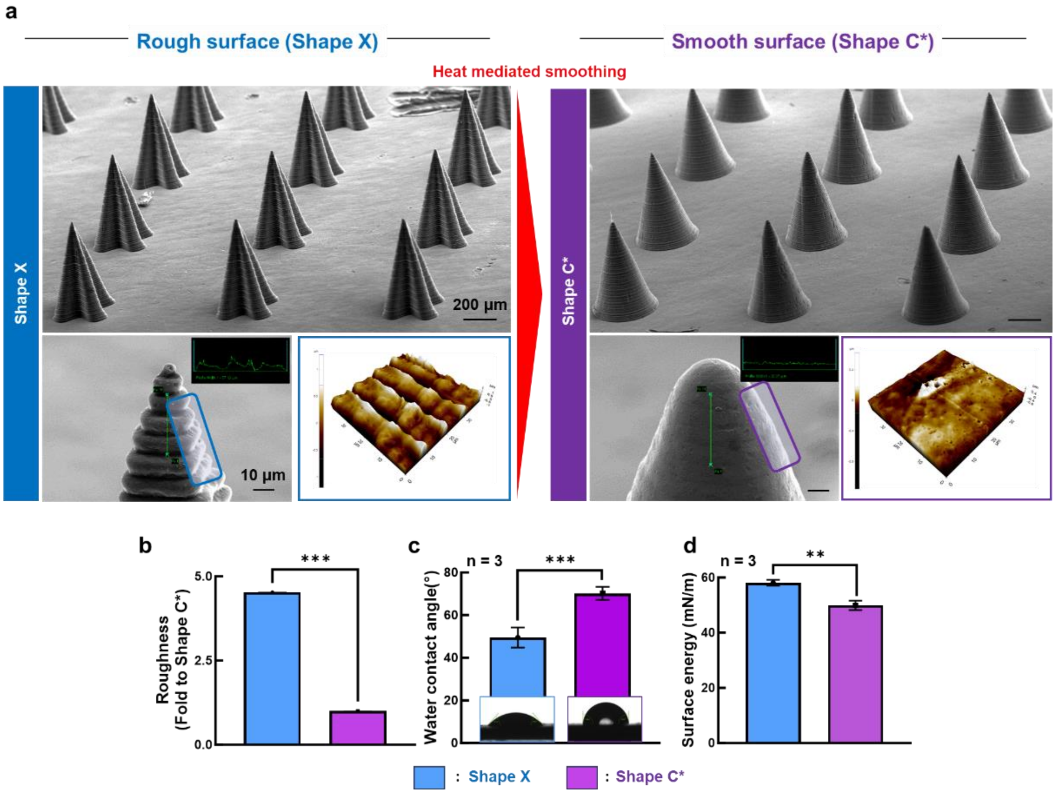

Figure 7. Surface properties of Shape X and Shape C*. Surface structures were analyzed using (a) SEM and AFM. AFM analysis also provided (b) surface roughness measurements. To assess GelMA adhesion capability, (c) water contact angle and (d) surface energy were measured. All data are presented as mean ± S.D. (n = 3–5). $*p < 0.05$, $**p < 0.01$, $***p < 0.001$ between the indicated groups.

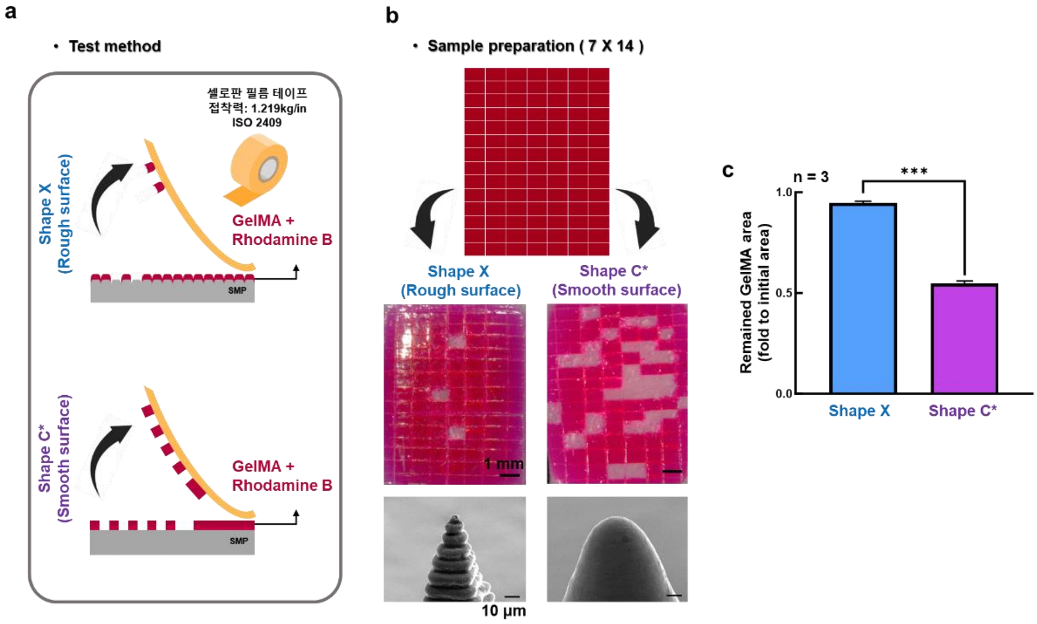

Figure 8. Evaluation of GelMA adhesion on different microneedle surfaces using a modified cross-cut adhesion test. (a) Schematic of the test procedure in the Shape X (rough surface) and Shape C* (smooth surface) states. (b) RhoB-labeled GelMA-coated microneedle arrays were subjected to tape peeling after a grid-patterned incision. (c) Measurement of the remaining GelMA area after peeling off. All data are shown as the mean ± S.D. (n=3) *$p < 0.05$, **$p < 0.01$, and ***$p < 0.001$ between the indicated groups.

3.4. Drug release and skin penetration performance through of SMN

Previously, the shape-transforming capability of the SMN was shown through structural and dimensional analysis. To investigate whether this self-transformation directly enhances drug delivery performance, an agar-based hydrogel model was developed using methylene blue to simulate soft tissue environments [36] (**Fig. 9-a**). The SMN was inserted into the hydrogel under two conditions: with and without heat-induced self-transformation. Time-lapse images revealed that rapid diffusion of methylene blue into the gel occurred only when self-transformation was triggered by brief heating at 45 ℃ for 10 s, indicating that the structural change improves delivery efficiency **(Fig. 9-b)**. To assess the extent of this enhancement, microneedle penetration depth was tracked over time **(Fig. 9-c)**. The self-transformed group consistently achieved greater insertion depth than the non-transformed group, suggesting improved mechanical penetration. In addition, peak intensity measurements of methylene blue demonstrated enhanced diffusion efficiency in the shape-recovered group. At 30 minutes, the peak intensity reached approximately 9.6 a.u. in the self-transforming (+) group, significantly higher than the 7.2 a.u. observed in the non-transforming (–) group ($p < 0.001$). These results support the role of self-transformation in facilitating deeper tissue penetration and more effective molecular transport **(Fig. 9-d)**.

Penetration performance was further analyzed based on three geometric parameters known to correlate with insertion efficiency: apex angle, tip surface area, and sharpness index [37] **(Fig. 10-a)**. Apex angles remained consistent between Shape X and Shape X*, confirming structural stability during GelMA coating by SEM imaging **(Fig. 10-b)**. However, tip surface area decreased after coating, leading to more focused pressure at the tip **(Fig. 10-c)**. The sharpness index, calculated from the tip radius of curvature, was marked higher in Shape X*, indicating enhanced tip sharpness and penetration potential **(Fig. 10-d)**.

These findings suggest that the transition from Shape X to Shape X* improves mechanical penetration performance, providing the SMN more effective for transdermal delivery. The skin penetration performance of the SMN was also evaluated in an *ex*-vivo rabbit skin model **(Fig. 11-a)**. Clear puncture marks appeared after insertion, indicating successful skin penetration. Histological analysis confirmed that the microneedles penetrated through the stratum corneum into the dermal layer, where the GelMA remained localized **(Fig. 11-b)**. Trypan blue staining was used to visualize penetration sites, producing blue dots that matched the microneedle array pattern **(Fig. 11-c)**. This indicated effective skin disruption, as trypan blue selectively stains areas where cell membranes are compromised.

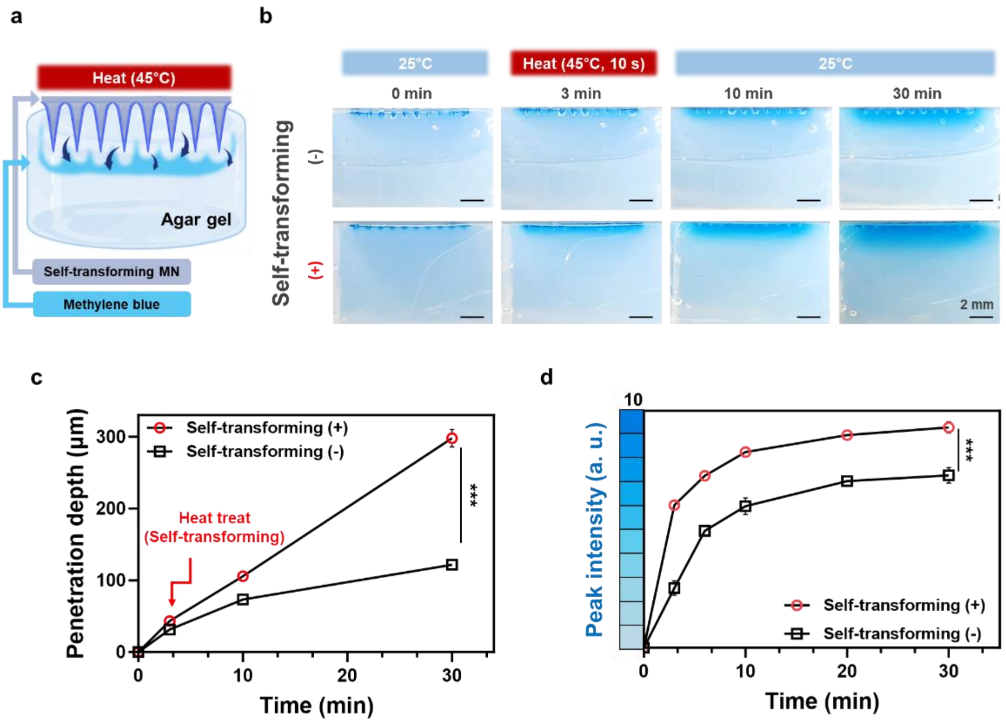

Figure 9. In vitro drug delievery performance. (a) Schematic diagram showing the in vitro release behavior of the self-transforming MN in the agarose hydrogel. (b) Photographs of cross-sectional comparing drug permeation across two different conditions: self-transforming/no shape self-transforming. Scale bar, 2mm for all panels. Penetration depth of the drug (c) and peak intensity (d) of the SMN across different time points. All data are shown as the mean ± S.D. (n = 6) *p < 0.05, **p < 0.01, and ***p < 0.001 between lined groups.

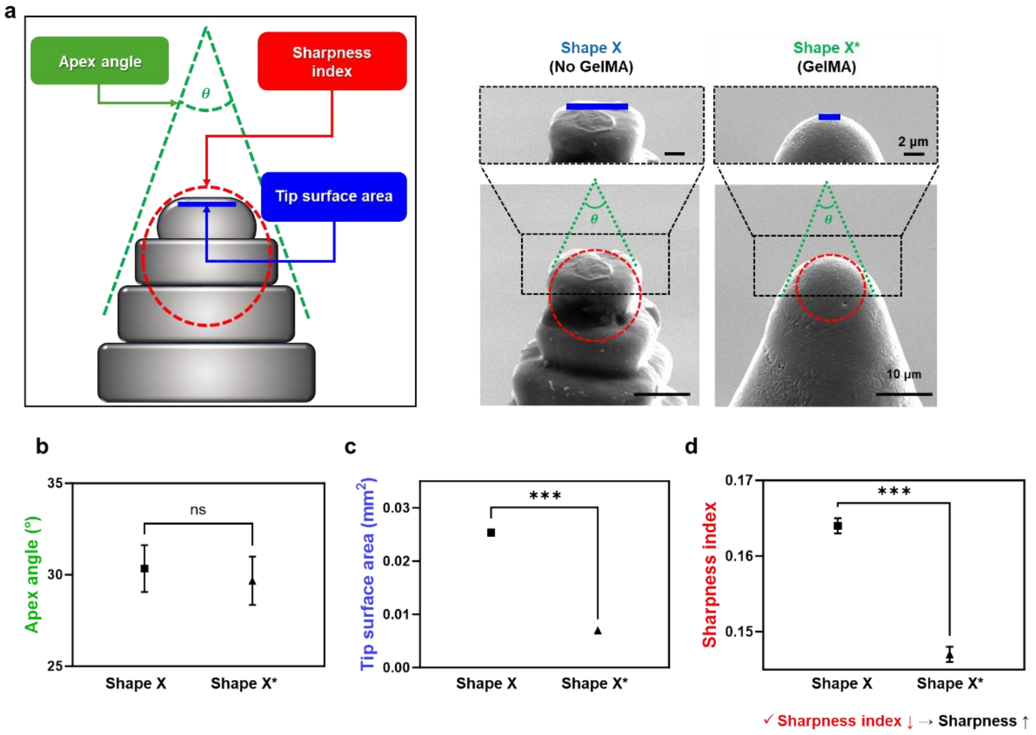

Figure 10. Tip geometry analysis of Shape X and Shape X*. (a) Schematic and SEM images illustrating apex angle, tip surface area, and sharpness index for evaluating penetration performance. Comparison of tip sharpness between Shape X and Shape X*, based on (b) apex angle (°), (c) tip surface area (mm^2) and (d) sharpness index. All data are shown as the mean ± S.D. (n=5) $*p < 0.05$, $**p < 0.01$, and $***p < 0.001$ between indicated groups.

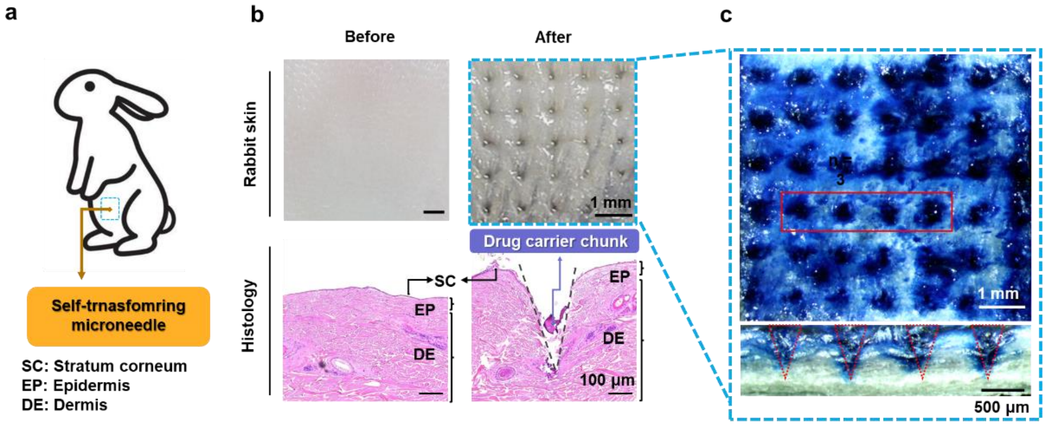

Figure 11. Evaluation of skin penetration with SMN and drug delivery using rabbit skin. (a) Schematic illustration of SMN to rabbit skin for *ex vivo* penetration analysis. (b) Photographic and histological images of skin before and after SMN insertion, showing mechanical penetration and localization of drug carrier in the dermal layer. Visualization of skin penetration using trypan blue staining (c), which highlights damaged sites.

3.5. Dual-loaded drug delivery performance with self-transforming

To establish a time-controlled release system using SMN, in vitro drug release studies were examined in a saline (**Fig. 12-a**). The microneedle was preloaded with FSH and hCG to enable dual-phase release regulated by self-transformation. FSH was gradually released over 72 h while the SMNs remained in their initial configuration as Shape X. Upon thermal activation, the SMNs transformed into Shape C*, triggering a burst release of hCG from the inner compartment within 24 h. To optimize temporal control, GelMA degradation behavior was evaluated under varying crosslinking point and polymer concentrations **(Fig. 12-b)**. At 10% crosslinking point and 5% (w/v) polymer concentration, the hydrogel fully degraded within 24 hours and was thus applied to the hCG layer to enable rapid release. In contrast, increasing the concentration to 10% (w/v) extended degradation to 72 h, making it suitable for FSH loading to support sustained release. Drug release kinetics were analyzed by ELISA **(Fig. 12-c)**. FSH exhibited a gradual release over 72 h, whereas hCG was rapidly released within 24 h following shape transformation. These findings demonstrate that shape memory–driven transformation, in combination with tunable GelMA degradation rate, enables programmable and sequential delivery of dual hormonal agents.

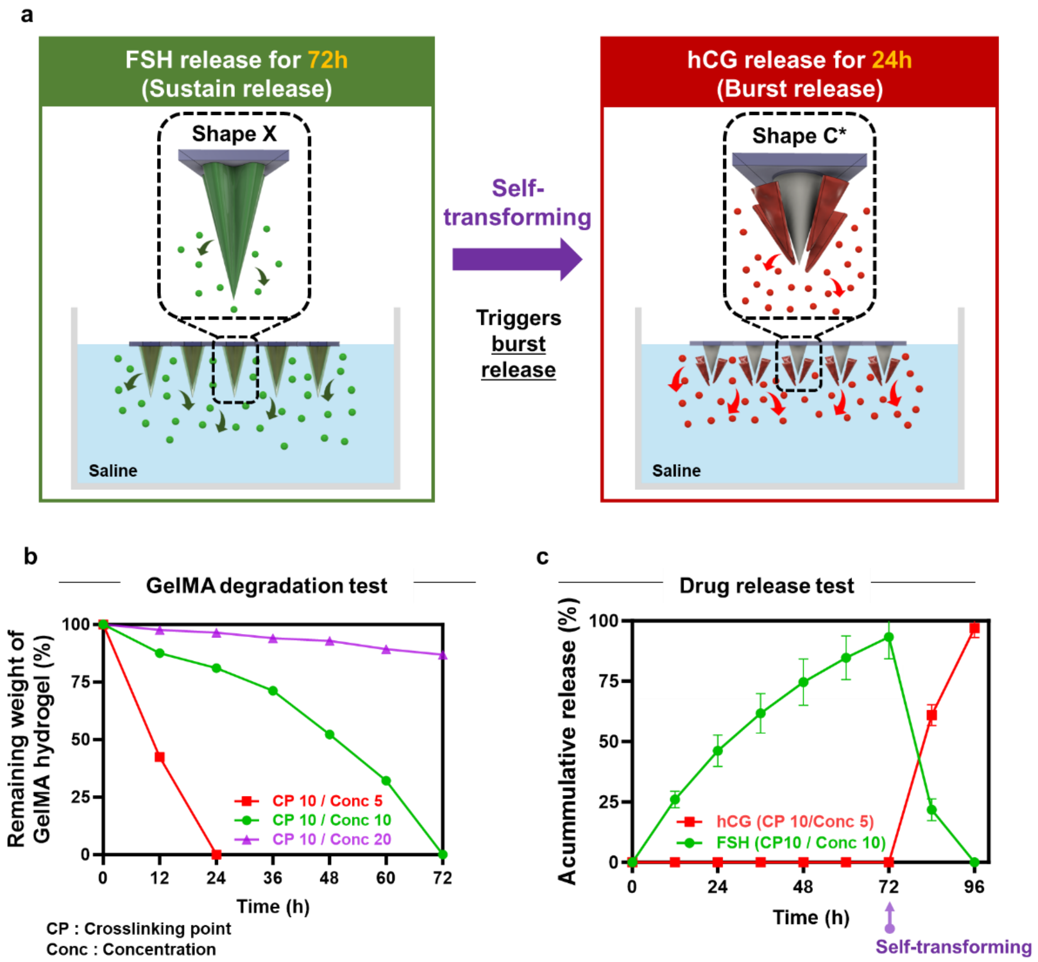

Figure 12. Controlled release of drug delivery with SMN (a) Schematic illustration of the in vitro drug delivery process of the SMN. GelMA degradation characteristics (b) depending on crosslinking point (CP) and concentration. (c) Statistical analysis of the cumulative amount of FSH and hCG permeated into the medium solution.

4. DISCUSSION

In this study, we developed a self-transforming microneedle (SMN) system based on shape memory polymers (SMPs) for sequential hormone delivery. By utilizing thermally induced shape recovery, the system was designed to achieve time-controlled release of two gonadotropins—FSH and hCG—within a single device. The platform offers a potential solution to the limitations of conventional hormone therapy, which often requires multiple injections and is associated with low patient compliance.

The SMN was programmed to remain in a deformed shape (Shape X), where the surface retained ridges and grooves generated during 3D printing. In this configuration, FSH was gradually released from the outer GelMA layer over 72 hours. Upon mild heating to 45 °C, the microneedle recovered its original conical shape (Shape C*), triggering structural opening of the inner compartment and resulting in the rapid release of hCG within 24 hours. This dual-phase release strategy mirrors the biological sequence of follicular stimulation followed by ovulation induction and enables programmable delivery without external injection or multiple devices.

The surface morphology of the SMN played a key role in modulating hydrogel adhesion and drug release. In the pre-recovered state (Shape X), the roughened surface provided higher surface energy, enhancing the retention of the GelMA coating. After shape recovery, the surface became smoother, facilitating hydrogel detachment and burst release of the encapsulated hormone. These results highlight the importance of dynamic surface modulation through mechanical transformation in regulating material–hydrogel interaction and release kinetics.

The mechanical performance and release efficiency of the SMN were validated through in vitro and *ex vivo* experiments. In a tissue-mimicking agarose gel model, methylene blue diffusion occurred more extensively and rapidly in thermally activated microneedles, demonstrating that shape transformation significantly enhanced delivery depth and spread. Furthermore, *ex vivo* insertion into rabbit skin showed accurate microneedle penetration aligned with the array pattern, and trypan blue staining confirmed successful delivery into the targeted tissue regions. These results support the feasibility of the SMN system as a transdermal delivery platform with mechanical and functional integrity.

Nevertheless, several limitations must be addressed for future *in vivo* translation. First, while thermal activation was easily controlled in vitro and *ex vivo*, precise heat delivery *in vivo* may be affected by local tissue temperature, blood flow, and physiological variability. Although the transformation was designed to occur at a relatively low temperature (45 °C), the practical method of localized heating and its safety require further evaluation in animal models. Second, while GelMA degradation rates were tunable through crosslinking density and concentration, enzymatic degradation and immune responses *in vivo* could alter release timing. Additional studies are necessary to characterize degradation behavior and optimize release profiles under physiological conditions.

Despite these challenges, the SMN system demonstrates appreciable potential for broader therapeutic applications. Although this study focused on hormone delivery, the concept can be extended to other fields that require multi-phase or on-demand drug administration, such as chemotherapy, regenerative medicine, or vaccine delivery. The use of microneedles enables minimally invasive, localized treatment while reducing systemic side effects and improving user compliance.

In conclusion, this work presents a novel drug delivery strategy that integrates mechanical transformation and programmable release within a single microneedle device. By enabling dual-phase release via shape memory control, the SMN platform offers a promising approach for patient-friendly, temporally optimized drug delivery. Future *in vivo* investigations into safety, long-term performance, and therapeutic efficacy will be essential for advancing this technology toward clinical applications.

.

5. CONCLUSTION

In this study, a SMN platform based on SMP was developed to achieve time-programmed, sequential delivery of two gonadotropin hormones, FSH and hCG. By integrating thermos-responsive SMP with GelMA hydrogel coatings of tunable degradation kinetics, the platform enabled dual-phase hormone release controlled by self-transformation. FSH was released gradually over 72 h from the outer GelMA layer in the before self-transformation (Shape X), while thermal activation induced rapid release of hCG within 24 h during the self-transform to Shape C*. This strategy mirrors clinical hormone therapy protocols that require sequential follicular stimulation and ovulation induction.

Surface properties of the SMN were shown to modulate hydrogel adhesion and detachment, with rougher surfaces in the Shape X state enhancing GelMA coating stability and smoother surfaces after self-transformation promoting controlled release. In vitro and *ex vivo* penetration were assessed SMN capability to achieve mechanically effective skin insertion, time-dependent drug release, and temperature-triggered actuation. Quantitative analysis demonstrated that mechanical self-transformation substantial enhanced delivery depth and drug diffusion.

This SMN platform addresses medical unmet needs in continuous drug treatment by reducing the number of injections and enabling localized, on-demand drug release. While current results validate the system under controlled laboratory conditions, further *in vivo* studies are required to evaluate its pharmacokinetics, biocompatibility, and therapeutic efficacy in physiologic environments. Additionally, long-term safety and potential applications for other sequential drug delivery contexts—such as cancer therapy or regenerative medicine—remain promising directions for future exploration.

References

1. Brugo-Olmedo, S., et al. "Definition and Causes of Infertility." *Reproductive Biomedicine Online*, vol. 2, no. 1, 2001, pp. 41–53.
2. Blundell, R. "Causes of Infertility." *International Journal of Molecular Medicine and Advanced Sciences*, vol. 3, no. 1, 2007, pp. 63–65.
3. Rafael, F. "Clinical Management of Uterine Factors in Infertile Patients." *Seminars in Reproductive Medicine*, vol. 3, no. 2, 1985, pp. 149–167.
4. Ioannis, E. "Ovulation Induction: A Mini Review." *Human Reproduction*, vol. 20, no. 10, 2005, pp. 2688–2697.
5. Holzer, H., et al. "A New Era in Ovulation Induction." *Fertility and Sterility*, vol. 85, no. 2, 2006, pp. 277–284.
6. Fatemi, H., et al. "Dose Adjustment of Follicle-Stimulating Hormone (FSH) During Ovarian Stimulation as Part of Medically-Assisted Reproduction in Clinical Studies: A Systematic Review Covering 10 Years (2007–2017)." *Reproductive Biology and Endocrinology*, vol. 19, no. 1, 2021, article 68.
7. Lispi, M., et al. "Follicle-Stimulating Hormone Biological Products: Does Potency Predict Clinical Efficacy?" *International Journal of Molecular Sciences*, vol. 24, no. 10, 2023, article 9020.
8. Van Tilborg, T.C., et al. "The OPTIMIST Study: Optimisation of Cost Effectiveness Through Individualised FSH Stimulation Dosages for IVF Treatment. A Randomised Controlled Trial." *BMC Women's Health*, vol. 12, 2012, article 29.
9. Zeleznik, A.J., et al. "Development-dependent Responses of Ovarian Follicles to FSH and hCG." *American Journal of Physiology*, vol. 233, no. 3, 1977, pp. E229–E234.
10. Rosa, A.C., et al. "Effectiveness and Safety of Gonadotropins Used in Female Infertility: A Population-based Study in the Lazio Region, Italy." *European Journal of Clinical Pharmacology*, vol. 78, no. 7, 2022, pp. 1185–1196.
11. Lunenfeld, B. "Historical Perspectives in Gonadotrophin Therapy." *Human Reproduction Update*, vol. 10, no. 6, 2004, pp. 453–467.
12. Lunenfeld, B. "Gonadotropin Stimulation: Past, Present and Future." *Reproductive Medicine and Biology*, vol. 11, no. 1, 2011, pp. 11–25.
13. Kumar, P., et al. "Ovarian Hyperstimulation Syndrome." *Journal of Human Reproductive Sciences*, vol. 4, no. 2, 2011, pp. 70–75.
14. Lunenfeld, B., et al. "The Development of Gonadotropins for Clinical Use in the Treatment of Infertility." *Frontiers in Endocrinology*, vol. 10, 2019, article 429.
15. Rodger, M.A., and L. King. "Drawing Up and Administering Intramuscular Injections: A Review of the Literature." *Journal of Advanced Nursing*, vol. 31, no. 3, 2000, pp. 574–582.
16. Karpuz, M., and A.Y. Özer. "Syringes as Medical Devices." *FABAD Journal of Pharmaceutical Sciences*, vol. 41, 2016, pp. 27–37.

17. Sokolowski, C.J., et al. "Needle Phobia: Etiology, Adverse Consequences, and Patient Management." *Dental Clinics of North America*, vol. 54, no. 4, 2010, pp. 731–744.
18. Ha, H., et al. "Shape-Configurable Mesh for Hernia Repair by Synchronizing Anisotropic Body Motion." *Small*, vol. 19, no. 47, 2023, 2303325.
19. Shin, Y. C., et al. "Development of a Shape-Memory Tube to Prevent Vascular Stenosis." *Advanced Materials*, vol. 31, no. 44, 2019, 1904476.
20. Park, J. Y., et al. "Nasolacrimal Stent with Shape Memory as an Advanced Alternative to Silicone Products." *Acta Biomaterialia*, vol. 101, 2019, pp. 273–284.
21. Ha, H., et al. "Vascular Cast to Program Antistenotic Hemodynamics and Remodeling of Vein Graft." *Advanced Science*, vol. 10, no. 10, 2023, 2204993.
22. Avcil, M., and A. Çelik. "Microneedles in Drug Delivery: Progress and Challenges." *Micromachines*, vol. 12, no. 11, 2021, article 1321.
24. Jung, J.H., and S.G. Jin. "Microneedle for Transdermal Drug Delivery: Current Trends and Fabrication." *Journal of Pharmaceutical Investigation*, vol. 51, no. 5, 2021, pp. 503–517.
25. Faraji Rad, Z., et al. "An Overview of Microneedle Applications, Materials, and Fabrication Methods." *Beilstein Journal of Nanotechnology*, vol. 12, 2021, pp. 1034–1046.
26. Ohki, T., et al. "Mechanical and Shape Memory Behavior of Composites with Shape Memory Polymer." *Composites Part A: Applied Science and Manufacturing*, vol. 35, no. 9, 2004, pp. 1065–1073.
27. Yakacki, Christopher M., et al. "Strong, Tailored, Biocompatible Shape-Memory Polymer Networks." *Advanced Functional Materials*, vol. 18, no. 16, 2008, pp. 2428–2435.
28. Zhou, X. *et al.* "Biodegradable β-Cyclodextrin Conjugated Gelatin Methacryloyl Microneedle for Delivery of Water-Insoluble Drug." *Advanced Healthcare Materials*, vol. 9, no. 11, 2020, article no. 2000527.
29. Ashley, Gary W., et al. "Hydrogel Drug Delivery System with Predictable and Tunable Drug Release and Degradation Rates." *Proceedings of the National Academy of Sciences*, vol. 110, no. 6, 2013, pp. 2318–2323.
30. Lee, K. *et al.* "Laser-Responsive Shape Memory Device to Program the Stepwise Control of Intraocular Pressure in Glaucoma." *Advanced Functional Materials*, vol. 33, no. 35, 2023, article no. 2300264.
31. Yan, Qi, et al. "The Finite Element Analysis Research on Microneedle Design Strategy and Transdermal Drug Delivery System." *Pharmaceutics*, vol. 14, no. 8, 2022, article 1625.
32. Bae, Won-Gyu, et al. "Snake Fang–Inspired Stamping Patch for Transdermal Delivery of Liquid Formulations." *Science Translational Medicine*, vol. 11, no. 503, 2019, article eaaw3329.
33. Vigata, Marina, et al. "Gelatin Methacryloyl Hydrogels Control the Localized Delivery of Albumin-Bound Paclitaxel." *Polymers*, vol. 12, no. 2, 2020, article 501.
34. Zhang, J., et al. "Effects of Surface Roughness on Wettability and Surface Energy of Coal." *Frontiers in Earth Science*, vol. 10, 2023, article 1054896.
35. Bamorovat Abadi, Ghazaleh, and Majid Bahrami. "The Effect of Surface Roughness on Capillary Rise in Micro-Grooves." *Scientific Reports*, vol. 12, 2022, article 14867.

36. Shao, J., et al. "Self-Heating Multistage Microneedle Patch for Topical Therapy of Skin Cancer." *Advanced Materials*, vol. 36, no. 15, 2024, article 2308217.
37. Crofts, Stephanie B., et al. "How Do Morphological Sharpness Measures Relate to Puncture Performance in Viperid Snake Fangs." *Biology Letters*, vol. 15, 2019, article 20180905.

Abstract in Korean

자가형상복원 마이크로니들 기반 이중 약물 탑재 및 제어 방출 시스템

불임 치료는 반복적인 호르몬 주사와 투여 시점의 정밀한 조절이 요구되며, 이로 인해 환자에게 심리적·신체적 부담이 상당한 치료 방식이다. 본 연구에서는 이러한 한계를 극복하기 위해 자가형상복원 기능을 갖는 마이크로니들(SMN)을 기반으로 한 이중 약물 전달 시스템을 설계하였다. 이 시스템은 외층에 난포자극호르몬(FSH), 내층에 배란유도호르몬(hCG)을 탑재하고, GelMA 하이드로겔과 열 자극을 이용한 구조적 전환을 통해 약물 방출의 순서와 속도를 정밀하게 제어할 수 있도록 구성되었다. 특히, 형상 복원 전후의 surface roughness 변화를 통해 약물의 부착성과 탈리 특성까지 조절함으로써, 시간에 따라 단계적인 약물 방출을 유도하였다. 이러한 구조적·기능적 특성을 기반으로, in vitro 및 ex vivo 실험을 통해 마이크로니들의 삽입 성능, 약물 방출 특성, 그리고 생물학적 반응을 연속적으로 검증하였으며, 기존의 주사 기반 치료법을 대체할 수 있는 전례 없는 약물 전달 플랫폼의 가능성을 제시하였다.

핵심되는 말 : 마이크로니들, 형상기억고분자, 자가형상복원, 이중 약물 탑재, 제어 방출